Nanomagnetic intergrowths in Fe–Ni meteoritic metal: The potential for time-resolved records of planetesimal dynamo fields

James F.J. Bryson [a,*], Nathan S. Church [a], Takeshi Kasama [b], Richard J. Harrison [a]

[a] *Department of Earth Sciences, University of Cambridge, Downing Street, Cambridge CB2 3EQ, UK*
[b] *Center for Electron Nanoscopy, Technical University of Denmark, Kongens Lyngby, Denmark*

A B S T R A C T

Nanoscale intergrowths unique to the cloudy zones (CZs) of meteoritic metal display novel magnetic behaviour with the potential to reveal new insight into the early development of magnetic fields on protoplanetary bodies. The nanomagnetic state of the CZ within the Tazewell IIICD iron meteorite has been imaged using off-axis electron holography. The CZ is revealed to be a natural nanocomposite of magnetically hard islands of tetrataenite (ordered FeNi) embedded in a magnetically soft matrix of ordered Fe_3Ni. In the remanent state, each tetrataenite island acts as a uniaxial single domain particle with its [001] magnetic easy axis oriented along one of three ⟨100⟩ crystallographic directions of the parent taenite phase. Micromagnetic simulations demonstrate that switching occurs via the nucleation and propagation of domain walls through individual tetrataenite particles. The switching field (H_s) varies with the length scale of the matrix phase (L_m), with $H_s > 1$ T for $L_m \sim 10$ nm (approaching the intrinsic switching field for isolated single domain tetrataenite) and $0.2 < H_s < 0.6$ T for $L_m \sim 30$ nm. The reduction in H_s with increasing L_c is caused by exchange coupling between the hard tetrataenite islands and the soft magnetic matrix, which lowers the critical field for domain wall nucleation, providing an explanation for previously observed coercivity variations throughout the CZ. Non-random distributions of the tetrataenite easy axes are observed locally throughout the CZ, suggesting a magnetic field could have been present during nanostructure formation. This observation demonstrates the potential for stable chemical transformation remanent magnetisation to be encoded by the nanostructure, with variations in the proportions of the six possible magnetisation states reflecting the intensity and relative direction of the magnetic fields present during cooling. According to recent cooling models, the cooling rate of meteoritic metal originating near the surface of differentiated planetesimals was such that the magnetic signal across the CZ could potentially record dynamo field intensity and direction variations over time (10–100 Ma), which would enable events such as magnetic reversals and the decay of an asteroid dynamo to be observed.

© 2013 The Authors. Published by Elsevier B.V. Open access under CC BY license.

1. Introduction

An increasing body of paleomagnetic evidence suggests that, while molten, the cores of differentiated planetesimals generated magnetic dynamo fields with comparable strength to those of present-day Earth (Tarduno et al., 2012; Fu et al., 2012; Weiss et al., 2010). Meteoritic Fe–Ni metal has recently been shown to contain nanoscale magnetic intergrowths that are potentially reliable paleomagnetic recorders (Uehara et al., 2011). Here we present the first high-resolution magnetic images of these intergrowths within the Tazewell IIICD iron meteorite, and describe how their novel magnetic properties could enable a time-resolved record of the dynamo field to be captured by meteoritic metal originating from near-surface regions of a differentiated asteroid.

Iron meteorites are fragments of the solidified cores of differentiated planetesimals (Goldstein et al., 2009) and consist predominantly of Fe-rich Fe–Ni alloy. At high temperatures ($>900\,°C$) Fe–Ni adopts the face-centred cubic (fcc) phase, taenite. On cooling to $\sim500\,°C$, large lamellae (~50 μm wide in this study) of the magnetically soft Fe-rich body-centred cubic (bcc) phase kamacite nucleate and grow parallel to taenite {111} planes (Yang and Goldstein, 2005) (Fig. 1a). This process ejects Ni into the surrounding taenite, establishing concentration gradients that vary from 50% Ni at the kamacite/taenite interface to <25% Ni over a distance of ~5–10 μm (Reuter et al., 1987). With further cooling to $\sim320\,°C$, taenite close to the interface undergoes an atomic ordering transition, creating a ~1–2 μm wide rim of tetrataenite (FeNi) (Yang et al., 1997a) – a magnetically hard phase uniquely

* Corresponding author.
E-mail addresses: jfjb2@cam.ac.uk (J.F.J. Bryson), nc315@cam.ac.uk (N.S. Church), takeshi.kasama@cen.dtu.dk (T. Kasama), rjh40@esc.cam.ac.uk (R.J. Harrison).
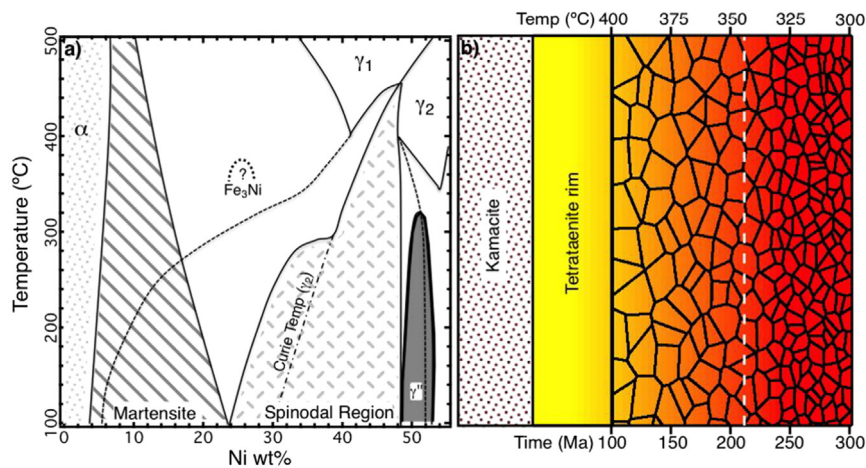
Fig. 1. Fe–Ni phase diagram and a schematic of meteoritic metal microstructure. (a) Low temperature phase diagram for the Fe-rich end of the Fe–Ni system, after Uehara et al. (2011). α – kamacite, γ_1 – paramagnetic taenite, γ_2 – ferromagnetic taenite, γ'' – tetrataenite. An approximate Fe_3Ni solvus has been added, with an ordering temperature from Dang and Rancourt (1996). (b) Schematic of the kamacite, tetrataenite rim and CZ. The relative sizes of the features are not to scale, although a qualitative decrease in CZ island diameter with increasing distance from the tetrataenite rim has been included. The colour represents the bulk composition established during kamacite lamellae formation; yellow: 50% Ni, red: 25% Ni. The local CZ age (relative to that of the asteroid) and formation temperature are included for a meteorite originating 10 km from the surface of a 200 km radius parent body (Tarduno et al., 2012). The dashed white line indicates the time and temperature of core solidification for such a body. (For interpretation of the references to colour in this figure, the reader is referred to the web version of this article.)

found in meteorites (Fig. 1a). Simultaneously, taenite neighbouring this rim spinodally decomposes (Fig. 1a), forming a 'cloudy zone' (hereafter CZ, Yang et al., 2007) of nanoscale tetrataenite islands embedded in an Fe-rich matrix. The spinodal decomposition temperature decreases as Ni concentration decreases (Fig. 1a), leading to a systematic decrease in the length scale of the island/matrix composite (Fig. 1b, Uehara et al., 2011). Tetrataenite has the tetragonal $L1_0$ structure (c/a $\sim$1.004) with its uniaxial magnetic easy axis along its c axis (Néel et al., 1964). This axis could be parallel to any of three $\langle 100 \rangle$ parent taenite axes, introducing the possibility that multiple magnetic easy axis orientations are present among the tetrataenite islands within the CZ. Several micrometres from the tetrataenite rim, an intergrowth of micron-sized laths of martensite and tetrataenite, known as plessite, forms. Plessite formation commences at $<500\,°C$, once the bulk composition of the meteorite reaches the martensite start temperature (Fig. 1a, Goldstein and Michael, 2006).

The high uniaxial magnetic anisotropy of tetrataenite (intrinsic switching field >2 T, Néel et al., 1964), coupled with the small size of the islands (which presumably places them in the proximity of the single-domain size range, Uehara et al., 2011) suggests the CZ has the potential be an excellent remanence carrier. However, the magnetic behaviour of the CZ has not previously been studied at the nanometre scale, and there are many factors that could affect its remanence carrying capabilities. First, the threshold size for the transition between single-domain and multidomain behaviour is unknown. Knowledge of this threshold, which also dictates the magnetic switching mechanism, is fundamental in assessing the properties of any potential remanence carrier. Second, the role of magnetostatic interactions between tetrataenite islands is unknown. Although the importance of such interactions in nanoscale oxide intergrowths is well established (Harrison et al., 2002; Evans et al., 2006; Feinberg et al., 2006), their influence on a magnetically hard phase such as tetrataenite is less certain. Third, Uehara et al. (2011) report a systematic variation in the coercivity of the CZ, from 0.4 T adjacent to the tetrataenite rim to >1 T among the finest tetrataenite islands. This behaviour is yet to be fully investigated, and could have a profound effect on the capability of the CZ to carry a stable remanence. Fourth, the structure, chemical composition and magnetic properties of the matrix phase are contentious, with evidence in support of various structures presented in the literature (e.g. bcc martensite, Goldstein et al.,

2009; fcc, Leroux et al., 2000; antitaenite, Rancourt et al., 1999). Exchange interactions between the tetrataenite islands and a potentially magnetic matrix phase are likely to have a dramatic effect on the overall magnetic properties of the intergrowth. Finally, the mechanism by which remanence is acquired during formation of the CZ is unknown. Determining this mechanism is essential if remanence measurements are to be properly interpreted. In this study, we attempt to address these factors and assess whether the CZ is likely to be a reliable source of paleomagnetic information. This is achieved by imaging the magnetic induction at the nanometre scale using off-axis electron holography (Harrison et al., 2002; Dunin-Borkowski et al., 2004) and inferring the magnetisation distribution among the tetrataenite islands using a combination of micromagnetic simulations and novel image simulation methods (Bryson et al., 2013). Having studied and understood the fundamentals of the CZ remanence, we then speculate as to the paleomagnetic information it is capable of providing, such as variations in the intensity and direction of dynamo fields on differentiated planetesimals during their first few hundred million years following accretion.

2. Methods

2.1. Experimental methods

The Tazewell IIICD iron meteorite was chosen for study based on previous electron microscopy studies (Goldstein et al., 2009; Reuter et al., 1987; Yang et al., 1997b) which demonstrate that the CZ had not been significantly affected by shock. A section of the meteorite was acquired from the Sedgwick Museum of Earth Sciences, University of Cambridge, UK. The meteorite section was mechanically polished and an electron transparent thin film then milled from the bulk material using a focused ion beam (FIB) of Ga ions with voltage 5 kV and final current of 700 pA (inset Fig. 2b). The film thickness varied between 50 and 100 nm. The beam energy was chosen to minimise the likelihood of inducing martensite formation (Maxwell et al., 1974) or inflicting damage to the thin film. The film contained kamacite, the tetrataenite rim and $\sim$7.5 µm of the CZ (Fig. 2). Scanning transmission electron microscopy (STEM) images, energy dispersive spectroscopy (EDS) maps, diffraction patterns and electron holograms were captured on an FEI Titan 300 kV TEM, and bright field images were captured
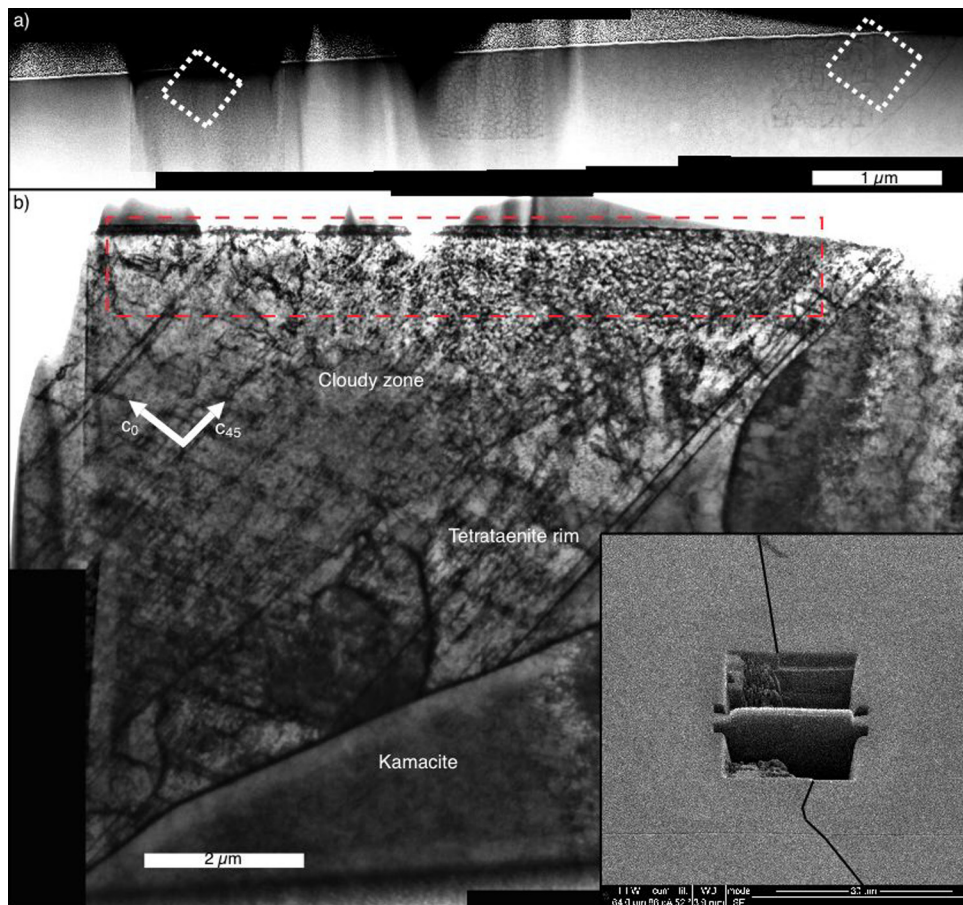
Fig. 2. Scanning transmission electron microscopy (STEM) and bright field (BF) images of the focused ion beam milled thin film. (a) STEM image of the top edge of the thin film (red dashed box in (b)). The tetrataenite islands are observable throughout the CZ. The coarse, intermediate and fine CZ regions have had their contrast digitally enhanced to highlight the island nanostructure. The dashed white boxes correspond to the regions where the coarse and fine region holography was performed. (b) BF image of the whole thin film. The kamacite, tetrataenite rim and CZ are all clearly identifiable. Shock twins visible as straight diagonal streaks can be seen. The inset in the bottom right of the image shows a scanning electron microscope image of the region of the bulk meteorite used to create the film with the kamacite/tetrataenite interface highlighted. (For interpretation of the references to colour in this figure, the reader is referred to the web version of this article.)

on an FEI Technai 300 kV TEM, both at the Centre for Electron Nanoscopy, Denmark Technical University, Copenhagen. Electron diffraction patterns were captured at various sample tilt angles, which indicate that the film is orientated normal to a [110] zone axis, thus two of the tetrataenite ⟨100⟩ axes are orientated 45° out of the sample plane, and the remaining axis is in the sample plane (included in Fig. 2b). Holography images were captured at remanence after the application of magnetic fields of ±200, ±500, ±800, ±1000 and ±2100 mT for the coarse region, and additionally of ±1200 mT for the fine region. These fields were generated by the microscope's objective lens, with the intensity controlled by the lens current. In-plane field components were introduced by tilting the sample ±25° about an axis perpendicular to the length and in the plane of the sample. This tilt orientation resulted in a dominant out-of-plane field component that retained its sign on tilting, and a weaker in-plane component parallel to the long edge of the film, which varied sign with that of the tilt. As the sign of the out-of-plane field component remained constant, only islands with an in-plane magnetic easy axis are expected to reverse magnetisation with the applied field.

Electron holograms were processed using the standard methods as outlined by Dunin-Borkowski et al. (2004). The holograms for the coarse region are presented with the mean inner potential (MIP) contribution to the phase shift included. As the sample thickness is relatively constant, and the tetrataenite and matrix phase are expected to have similar electronic properties, retaining the MIP has a negligible impact on the magnetic induction

maps for this region (Dunin-Borkowski et al., 2004). The fine region, on the other hand, contained artefacts resulting either from thickness variations introduced during FIB thinning or ripple contrast due to demagnetising effects (Dunin-Borkowski et al., 1998). To negate this effect, pairs of magnetically reversed phase maps were used to isolate any contributions to the phase shift that remain constant with the applied field (including the MIP contribution and thickness variations) according to the standard methods described by Dunin-Borkowski et al. (2004). This contribution was then subtracted from the original phase maps, leaving only the field-varying magnetic contribution to the phase shift. The holography signal is presented in the standard layout, with the colour relating to the direction (corresponding to the colour wheel) and the brightness relating to the intensity of the in-plane component of magnetic induction, integrated along the electron beam path.

2.2. Image simulations

To aid interpretation of the holography results, image simulations based on a range of trial magnetisation distributions were performed. Model magnetisation distributions were created by first generating a realistic three-dimensional nanostructure that mimicked the real CZ (Fig. 3). This was achieved by dividing a $256 \times 256 \times 30$ pixels simulation cell with 2 nm resolution per pixel into 50 equally sized boxes for the coarse region and 900 for the fine region. A pixel inside each box was chosen at random and
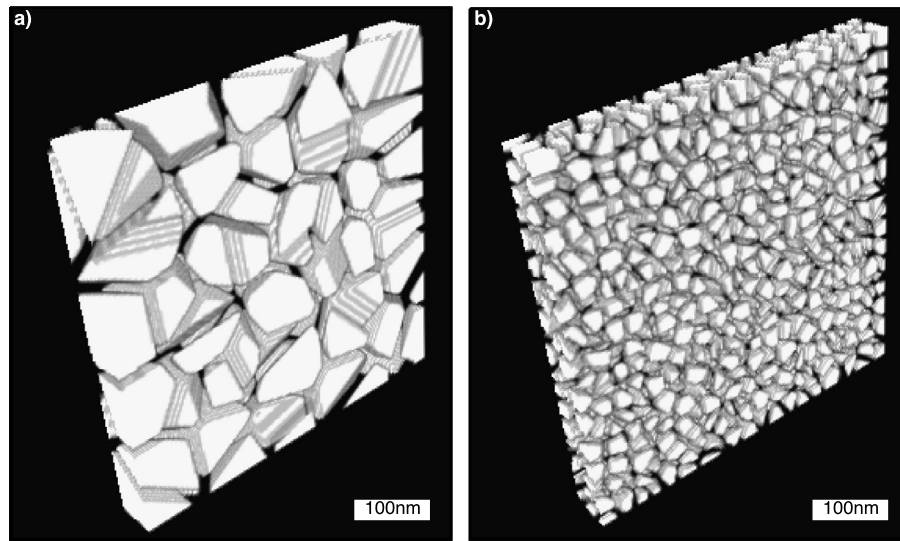
Fig. 3. Three-dimensional representations of the simulated (a) coarse and (b) fine CZ created using the method described in Section 2.2. The shapes, distribution and dimensions of the islands and matrix in both (a) and (b) match those observed experimentally. These nanostructures were used to generate the results in Figs. 5, 6, 7 and 8.

a Voronoi cell constructed around it. The Voronoi cells were then eroded to create a two-phase system of isolated cells embedded in a continuous matrix phase, with the dimensions, shapes and connectivity matching those observed experimentally. Each island was assigned to one of three mutually perpendicular easy axes, matching the crystallographic orientation of the experiments. Islands were modelled as uniformly magnetised parallel or antiparallel to their respective easy axes, with a magnetisation value of $M = 1300$ emu cm^{-3}. The matrix was modelled as either non-magnetic ($M = 0$ emu cm^{-3}) or as a soft magnet with $M = 1390$ emu cm^{-3}. In the magnetic case, each pixel of the matrix phase was assigned a magnetisation direction parallel to its nearest neighbouring island. This matrix magnetisation was then smoothed to account for the soft magnetic nature of this phase. If the islands on either side of a region of matrix have the same magnetisation direction, the intervening matrix is uniformly magnetised in that same direction. If the neighbouring islands are magnetised in different directions, the intervening matrix acts as the domain wall with smoothly varying moments. An increasing proportion of the in-plane easy axis islands, chosen at random, were reversed to mimic the effect of the field applied experimentally. The 3D magnetisation model was projected along the electron beam direction and the resulting 2D magnetisation map was used to calculate the electron optical phase shift using the ATHLETICS software suite (Bryson et al., 2013), based on the equations derived by Beleggia and Zhu (2003). The calculated phase maps are processed and presented in an identical way to the experimental ones to generate the corresponding maps of magnetic induction.

2.3. Micromagnetic simulations

Micromagnetic simulations were performed on a $128 \times 128 \times 32$ cell grid with 2 nm cell size using LLG micromagnetics (Scheinfein, 1997). This resolution ensured that the cell dimensions were less than the exchange length of tetrataenite. CZ nanostructures were created using Voronoi decomposition, as described above. Magnetic fields were applied in equivalent directions to those used experimentally. Micromagnetic parameters used for tetrataenite were: $M_s = 1300$ emu cm^{-3}, $A = 1.9$ μerg cm^{-1}, $K = 13\,700\,000$ erg cm^{-3} (Néel et al., 1964); and for Fe$_3$Ni: $M_s = 1390$ emu cm^{-3}, $A = 1.5$ μerg cm^{-1}, $K = 0$ erg cm^{-3} (James et al., 1999; Grabbe, 1940). Simulations were also performed with the saturation magnetisation value of the matrix phase set to zero,

so the effect of exchange coupling between phases could be investigated. The magnetocrystalline anisotropy of Ni$_3$Fe has been observed to be significantly lower than that of tetrataenite and hence the anisotropy of Fe$_3$Ni (which displays the same bonding and L1$_2$ cubic structure) was assumed to be zero. Islands were assigned to one of the three possible easy axis orientations in roughly equal proportions. Simulations were performed for both the coarse and fine CZ.

3. Results

3.1. Electron diffraction, EDS maps and STEM images

STEM images were captured along the entire length of the thin film (Fig. 2). These images display atomic number (Z) contrast, with brighter regions corresponding to the Ni-rich areas and the darker regions to the Fe-rich areas. The islands have ~90–100 nm diameters immediately adjacent to the tetrataenite rim, and reduce gradually in size to <10 nm with increasing distance from the rim (Fig. 4a and b). These values are in agreement with previous TEM studies performed on the same meteorite (Yang et al., 1997b). EDS maps of the coarse and intermediate CZ (Fig. 4c and d) demonstrate that the islands contain equal amounts of Fe and Ni, and that the matrix is roughly 75% Fe–25% Ni. Again, these values are in excellent agreement with previous studies (Leroux et al., 2000).

To investigate the crystal structure of the CZ, electron diffraction patterns were collected at various distances from the tetrataenite rim (Fig. 4e). Identical diffraction patterns were observed in all regions of the CZ. The diffraction pattern contains both primary reflections associated with the parent fcc lattice as well as a set of superlattice reflections caused by atomic ordering. The (100), (010) and (110) superlattice reflections labelled in Fig. 4e can each be explained as originating from tetrataenite islands with the L1$_0$ structure oriented in one of three possible crystallographic orientations, i.e. with the c axis oriented parallel to the [100], [010] and [001] directions of the parent taenite phase, respectively (simulated electron diffraction patterns are presented in the supplementary information). This interpretation would require that all three possible easy axis orientations are present in roughly equal proportions within the diffracting volume. An alternative explanation is that all three superlattice reflections originate (at least in part) from an ordered matrix phase with the L1$_2$ structure (i.e. Fe$_3$Ni with Ni atoms placed at the corners of the fcc unit cell). The
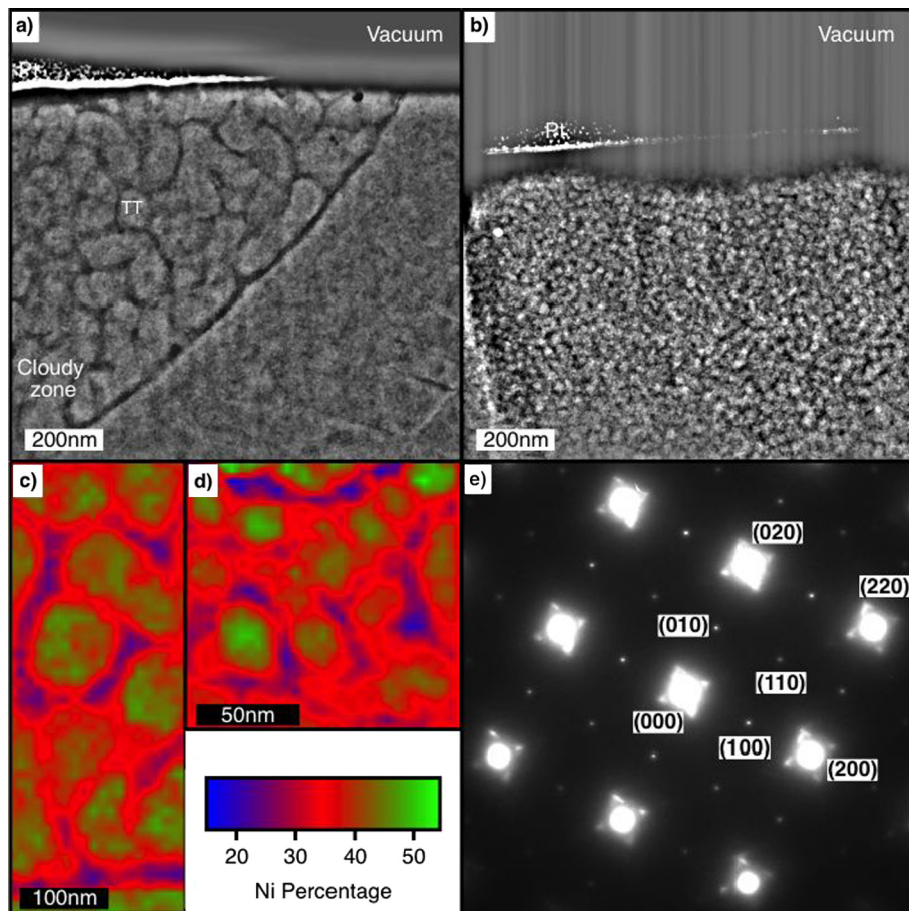
Fig. 4. Scanning transmission electron microscopy (STEM) images with enhanced contrast, diffraction patterns and energy dispersive spectra (EDS) from the CZ. (a) STEM image of the coarse CZ, showing the island/matrix nanostructure and tetrataenite rim. Pt – platinum; TT – tetrataenite. (b) STEM image of the fine CZ, starting at ∼5.5 μm from the tetrataenite rim. (c) EDS map of the coarse CZ. (d) EDS map of the CZ with medium sized islands, ∼2.8 μm from the tetrataenite rim. Both EDS maps display islands with 50% Ni:50% Fe and the matrix displays 25% Ni:75% Fe. (e) Diffraction pattern representative of both the coarse and fine CZ with peaks labelled.

principle reflections display satellite peaks consistent with double diffraction from a spinel structure, which are likely to originate from a thin layer of an iron oxide that coats the sample surfaces (Leroux et al., 2000).

3.2. Electron holography

Processed holograms showing the in-plane magnetic induction throughout the coarse CZ (immediately adjacent to the tetrataenite rim) are shown in Fig. 5. After application of a positive saturating field (Fig. 5c), the magnetic induction flows generally right to left (green), with localised patches flowing either top to bottom (yellow) or apparently out of the plane of the sample (black). There is little direct correspondence between the features observed in the induction map and the discrete island/matrix nanostructure observed using STEM (Fig. 5a). However with the application of a magnetic field, the induction is observed to change in discrete jumps, consistent with magnetic reversal of individual tetrataenite islands occurring over a range of magnetic fields. Full hysteresis cycles of experimental images are provided in the supplementary information, which reveals that switching begins at a field of ∼200 mT and is complete by 800 mT. Intricate magnetic induction signals are observed after application of fields close to the 'bulk' coercivity of the coarse CZ (∼500 mT; Fig. 5e), including localised patches flowing left to right (red), bottom to top (blue) and apparent flux closure structures reminiscent of magnetic vortices (Lappe et al., 2011). The induction measured after application of a negative saturating field (Fig. 5g) is not exactly antiparallel to that obtained in a positive saturating field (Fig. 5c), suggesting that not

all of the tetrataenite islands within the field of view reversed with the applied field. In particular, some localised patches of induction remain flowing from top to bottom (yellow) throughout the entire hysteresis cycle, indicating that some tetrataenite islands with easy axes oriented ∼45° out-of-plane did not change their magnetisation state at all during the experiment.

Processed holograms showing the in-plane distribution of magnetic induction throughout the fine CZ (∼5.5 μm from the tetrataenite rim) are shown in Fig. 6. After application of a positive saturating field (Fig. 6c) the magnetic induction flows uniformly from right to left (green), albeit with a distinct mottled texture that occurs on similar length scale to that observed in the corresponding STEM image (Fig. 6a). A full hysteresis cycle of experimental images is available in the supplementary information, which reveals that switching begins at ∼500 mT and ends at ∼1.2 T (i.e. at significantly greater field values than those observed in the coarse CZ). Again, intricate magnetic induction signals are observed after application of fields close to the 'bulk' coercivity of the fine CZ (∼800 mT), with localised patches of reversed (red) and apparently out-of-plane (black) flux. The induction measured after application of a negative saturating field (Fig. 6g) is exactly opposite to that obtained in a positive saturating field (Fig. 6c), although this result is inevitable given that reversed pairs of holograms were used to eliminate the MIP contribution in this case. The bright strip of uniform magnetic induction observed along the lower edge of the experimental maps in Fig. 6 (also visible in Fig. 5) corresponds to the original surface of the polished meteorite section. This ∼80–100 nm thick strip of soft magnetic material is a
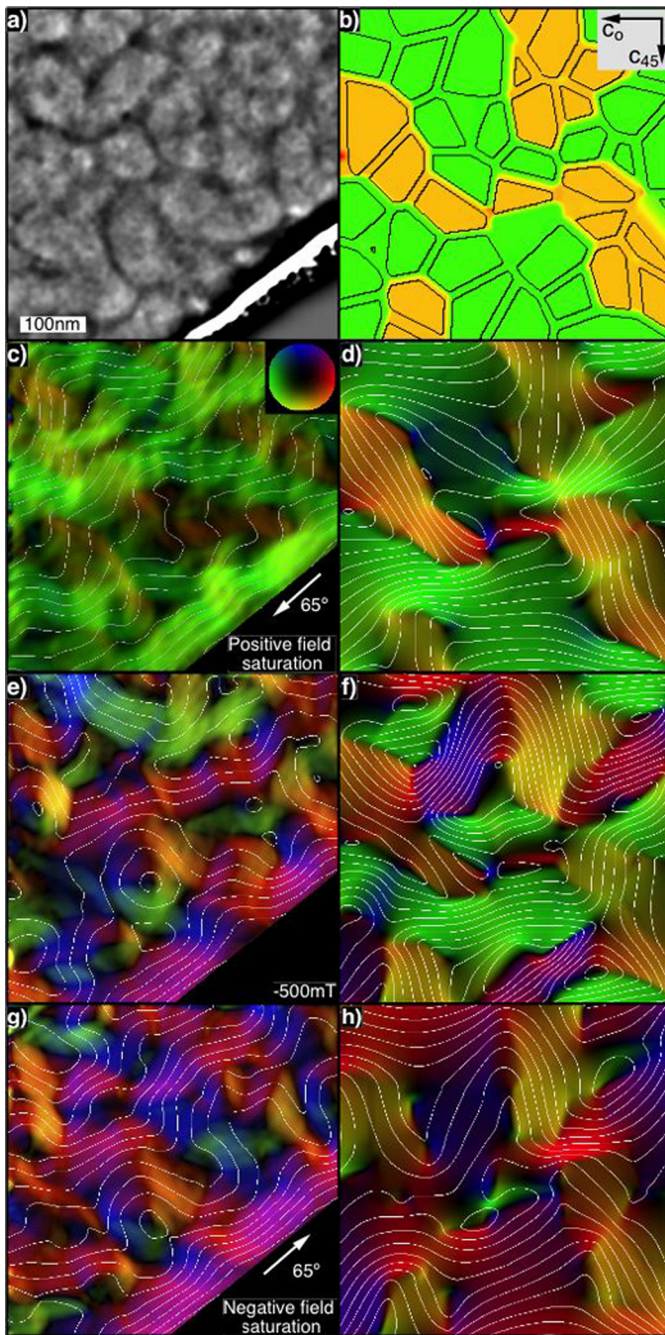
Fig. 5. Experimental and simulated electron holography images of the coarse CZ. (a) STEM image relating to experimental holography images. (b) Single layer of the simulated magnetic nanostructure used to model the course CZ with only two of the three possible magnetisation directions among the islands. The easy axis directions with their out-of-plane components are included as an inset in the top right of the image. (c), (e), (g) Remanent experimental holography images after applied field values and directions included in the image. (d), (f), (h) Simulated holography images corresponding to (c), (e) and (g) respectively. There is good agreement between the corresponding images. Note the yellow regions in both the experimental and simulated images remain present throughout all applied fields. Magnetisation and induction directions are indicated by the colour wheel included in (c). The applied field direction is included in (c) and (g), with the arrow providing the in-plane component and the annotation providing the out-of-plane component. The scale bar in (a) applies to all images. (For interpretation of the references to colour in this figure, the reader is referred to the web version of this article.)

Fig. 6. Experimental and simulated electron holography images of the fine CZ. (a) STEM image of the area studied. (b) Single layer of the simulated magnetic nanostructure. This simulation contained a paramagnetic matrix and only one of the possible easy axis directions among the islands. This easy axis distribution is to account for the lack of MIP in the experimental images which resulted in only the in-plane easy axis being visible in the final images. Vacuum was included in the top-left and bottom-right corners of the simulated images to introduce stray fields at the correct orientation. (c), (e) and (g) Remanent experimental holography images after applied field included in the image. (d), (f), (h) Simulated holography images corresponding to (c), (e) and g) respectively. There is good overall agreement between the experimental and simulated images, although it isn't possible to conclude that only one easy axis as present in this region due to the MIP removal. At most two easy axes are present. The scale bar in (a) applies to (c), (e) and (g), and the scale bar in (b) applies to (d), (f) and (h). The contour spacing in (e) has been decreased so the number of contours in the bulk of the experimental images remains approximately constant.

3.3. Image simulations

There are a number of factors that make it difficult to relate the experimental images of magnetic induction directly to the underlying magnetic state of the nanostructure. First, magnetic induction

sample preparation artefact caused by mechanical polishing prior to extraction of the TEM foil. Polishing induces a structural and chemical change in the surface of the sample, creating a magnetically soft layer with a coercivity <200 mT.
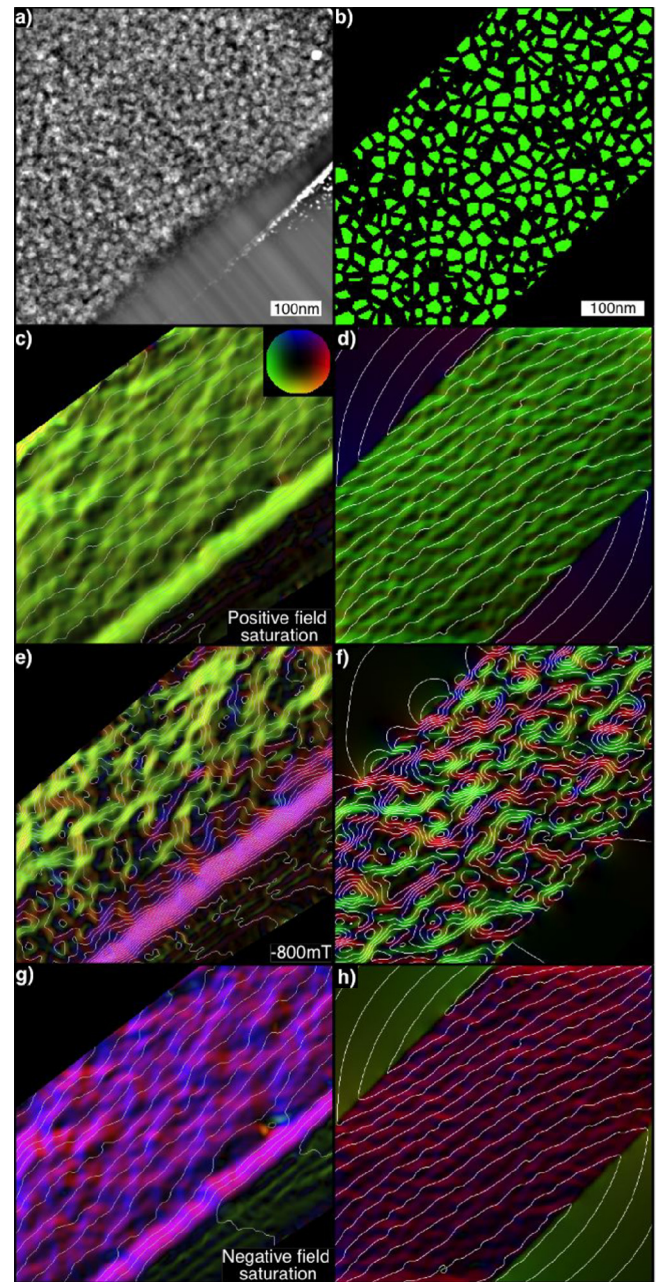
is given by the sum of the magnetisation (which we wish to determine), the internal demagnetising field and the magnetostatic stray fields generated by the islands and/or matrix, all of which have to be integrated along the electron beam path. Given that the islands are typically smaller than the thickness of the sample (very much smaller in the case of the fine CZ), the net induction is the result of multiple contributions coming from many overlapping islands. Second, due to the correction that was required to remove the MIP contribution from the fine CZ, any tetrataenite island that did not switch its magnetic state during the experiment does not contribute to the induction signal presented in Fig. 6 (this is not the case for the coarse CZ, where no correction for the MIP was necessary). Hence, regions in Fig. 6 that appear dark may be explained by either (i) a region that is not magnetic, (ii) a region that has a net out-of-plane induction, or (iii) a region that did not switch its magnetisation state in the positive and negative saturating fields. Third, the magnetic properties of the matrix phase are unknown, which makes it difficult to distinguish between induction caused by magnetostatic fields generated by the tetrataenite islands and induction associated with the intrinsic magnetisation of the matrix. Lastly, each tetrataenite island can have its easy axis along one of three mutually orthogonal easy axes, giving rise to rather intricate induction and return flux patterns.

To overcome some of these challenges, image simulations have been performed for a wide range of hypothetical magnetisation models and switching states for both the coarse and fine CZ (those found to not represent the experimental data are included in the supplementary information). Qualitative comparisons of the observed and simulated maps allow us to draw reasonable conclusions regarding the magnetic state of the sample, which are then tested using micromagnetic simulations (see next section). A full quantitative comparison of the simulated and experimental data sets was not possible as the simulated nanostructures were designed to match the general distribution of island sizes and shapes only, rather than provide an exact replica of the experimental nanostructure. Analysis was performed for either one, two or three easy axes distributed among the islands and with either a magnetic or non-magnetic matrix phase. Image simulations were started in the saturated state and an increasing proportion of islands with an in-plane easy axis were switched, mimicking the effect of an applied field in the experimental geometry (i.e. one where the out-of-plane component of applied field stays positive throughout).

For the coarse region, the simulated holography images that best relate to their experimental equivalents were those with single-domain islands populated with only two of the possible three easy axes, and a matrix saturation magnetisation value similar to that of tetrataenite (Fig. 5). The out-of-plane (yellow) and in-plane (green) regions appear in the experimental positive saturation field image to be organised in alternating diagonal stripes. Only by including this pattern in the simulations could the finer details of the experimental images be recreated and understood. For example, the blue areas observed in the experimental images after the application of larger negative fields (Fig. 5g and h) can be attributed to the constructive interference of stray fields generated by neighbouring islands at the boundary between the stripes of in- and out-of-plane easy axis islands.

For the fine region, the simulations demonstrate a dominance of the in-plane easy axis and that the unique mottled texture observed experimentally is most likely attributed to a reduced matrix saturation magnetisation value (Fig. 6). This conclusion was confirmed by comparison with holograms without their MIP removed (see supplementary information). The holography data cannot rule out the presence of a second easy axis orientation, but does not support the presence of all three easy axes with equal proportions.

Unlike the coarse CZ, there appears to be no distinguishable organisation to the positions of the islands in the fine CZ. No experimental image for either region displays field-invariant blue areas, implying that at most only one of the two possible easy axes with an out-of-plane component is found among the islands in either region. Thus, the holography signal in both regions consists of islands populated with magnetisation directions corresponding to at most two of the three possible easy axis orientations, and the saturation magnetisation value of the matrix appears to decrease with increasing distance from the tetrataenite rim.

Groups of neighbouring islands with the same magnetisation direction in the coarse region simulations tend to demonstrate more uniformity, both in direction and intensity, than in those observed experimentally (Fig. 5). This uniformity is due to difficulties in modelling the magnetically soft nature of matrix phase without full micromagnetic simulations (which were not possible to perform for this field-of-view at the required resolution). The model implemented in this study can result in matrix moments that are overly inclined to retain the direction of the islands they surround (especially if the neighbouring islands have the same magnetisation direction), resulting in the uniformity observed in the simulated images.

The induction direction in the fine region does not correspond to an easy axis direction, and is instead parallel to the sample edge (Fig. 6). This behaviour could be recreated in the simulations by substituting vacuum into two corners of the simulation grid, suggesting that the induction orientation is influenced by stray fields emanating from the sample itself. This region also displayed a significant thickness ramp, which will enhance the influence of these fields.

3.4. Micromagnetic simulations

The results of the micromagnetic simulations show that the majority of islands are single domain (Fig. 7). The magnetisation direction of the matrix depends on the state of the two closest islands: if the islands are magnetised parallel to each other, the matrix adopts a similar magnetisation direction; if adjacent islands are magnetised in different directions, the magnetisation of the matrix varies smoothly from one direction to the other. This configuration corresponds to a local energy minimum, and is also the general form of the magnetic configuration used in the image simulations. The simulations were performed in a vacuum, which creates demagnetising fields that would not have been present in reality. These demagnetising fields caused magnetic switching at unexpectedly low field values, especially for islands at the edges of the simulation cell. For example, the coarse CZ simulation with a magnetic matrix displays two islands with a reversed magnetisation at zero applied field, which has the effect of widening the switching region. Island reversal at all field values was achieved by nucleation and propagation of magnetic domain walls. Once a wall enters an island it sweeps through its entire volume immediately. In simulations containing a magnetic matrix, these domain walls formed first in the matrix phase and then push their way into the islands. Island switching occurs at a significantly reduced value in the coarse region than in the fine region, in good agreement with the experimental observations. Simulations with a non-magnetic matrix display switching at much higher fields than those observed experimentally (Fig. 8). The observed range of tetrataenite magnetic switching fields can only be recreated with a magnetic matrix phase, whereby the nucleation of domain walls in the hard islands is aided by exchange coupling to the soft matrix.
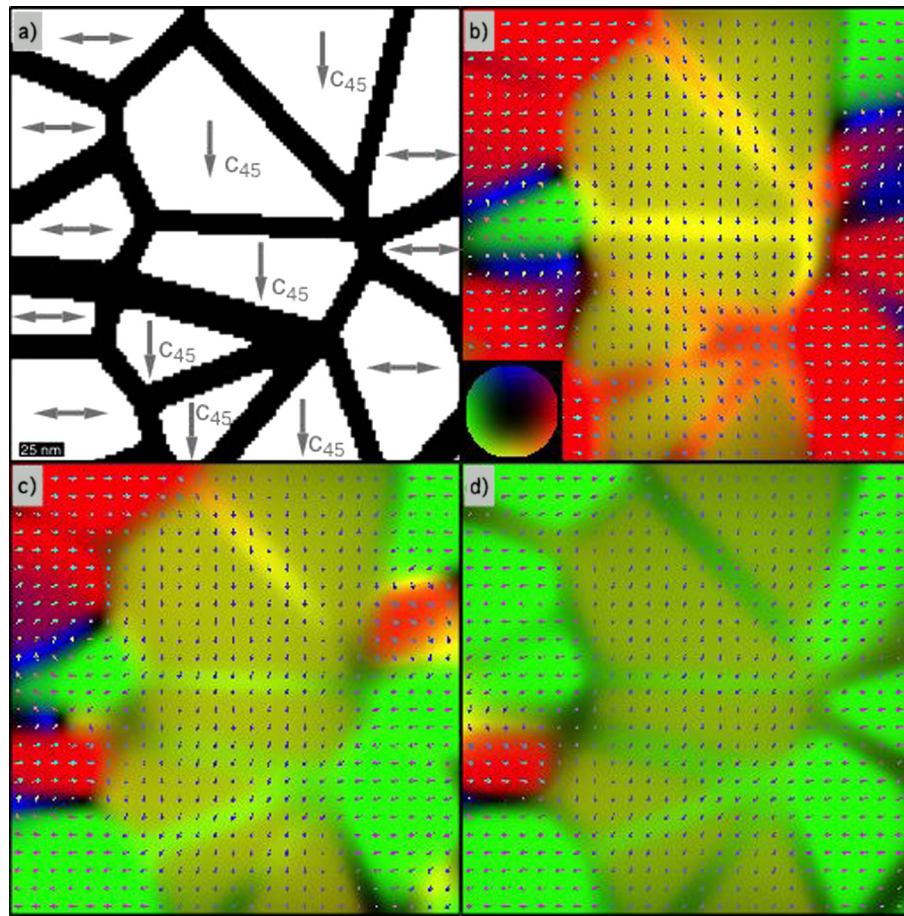
Fig. 7. Micromagnetic simulation results for the coarse CZ. (a) Simulated nanostructure used in the simulations. The easy axis direction for each island is included as a grey arrow. (b) Micromagnetic simulation result at 0 T after the application of a negative saturation field in the same orientation relative to the easy axes as those applied experimentally. The majority of in-plane magnetisation islands appear red although some reversal is observed at 0 T resulting from stray fields generated by the simulation cell itself. Most islands appears to be single domain with the only exceptions being at the very edge of the simulation cell where stray fields can lead to unrealistic effects. The magnetisation direction is indicated by the colour (relating to the colour wheel) and the arrows. (c) Result after the application of a −0.36 T field. Domain walls nucleate and propagated through some islands. (d) Result after the application of a −1 T field showing the majority of islands with a reversed magnetisation direction. Again, reversal is not complete throughout all islands due to stray fields. Note that none of the islands with an out-of-plane magnetisation component (central stripe) reversed with the applied field. (For interpretation of the references to colour in this figure, the reader is referred to the web version of this article.)

4. Discussion

4.1. Structure of the matrix phase

Our analysis of the electron holography results supports the conclusion that only two easy axes are present in each of the regions studied. This observation does not preclude the presence of all three easy axes within other regions that are outside the field-of-view. As described in Section 3.1, this analysis supports an interpretation of the electron diffraction patterns whereby the presence of all three superlattice reflections is due to a combination of tetrataenite with the $L1_0$ structure and an ordered Fe_3Ni matrix phase with the $L1_2$ structure. This interpretation is also consistent with the EDS results (Fig. 4c and d), which demonstrate a chemical composition of 25% Ni, and is further supported by image simulations of the holography results and micromagnetic simulations, which indicate that the matrix phase is magnetic. Density functional theory calculations (James et al., 1999) suggest that ordered Fe_3Ni should display a saturation magnetisation value similar to that of tetrataenite (1390 emu cm^{-3} and 1300 emu cm^{-3} respectively), whereas a disordered fcc phase with this bulk composition would be paramagnetic at room temperature.

Fe_3Ni has not previously been identified in nature or synthesised in the laboratory, presumably due to slow diffusion rates below the proposed ordering temperature (320 °C) and the thermo-

dynamic favourability of bcc martensite for disordered 25% Ni–75% Fe at room temperature (Howald, 2003). The existence of ordered Fe_3Ni has, however, been predicted by Monte Carlo simulations (Dang and Rancourt, 1996). The majority of previous TEM experimental observations (e.g. Goldstein et al., 2009; Reuter et al., 1987; Leroux et al., 2000; Yang et al., 1997b) suggest the matrix is comprised of bcc martensite. One previous TEM study (Leroux et al., 2000) observed an fcc matrix phase in conjunction with a bcc phase, and the authors suggest that strain from the tetrataenite islands can suppress the martensitic transition so fcc taenite remains present to uncharacteristically low temperatures, allowing Fe_3Ni to form upon ultra-slow cooling. It is possible to explain the reduced magnetisation of the fine-region matrix phase suggested by the image comparisons through a reduced degree of chemical order. The fine region spinodally decomposed at lower temperatures than the coarse region, hence it is feasible that the matrix is yet to reach full chemical order. The diffraction pattern of the fine region still contains all three superlattice reflections, however, requiring the matrix to be at least partly chemically ordered. We suggest that the bcc matrix phase observed in the previous studies is the result of chemical disordering resulting from sample preparation techniques (Maxwell et al., 1974), similar to the process that occurs at the sample surface creating the magnetically soft layer observed in the holography images (Morito et al., 2003).
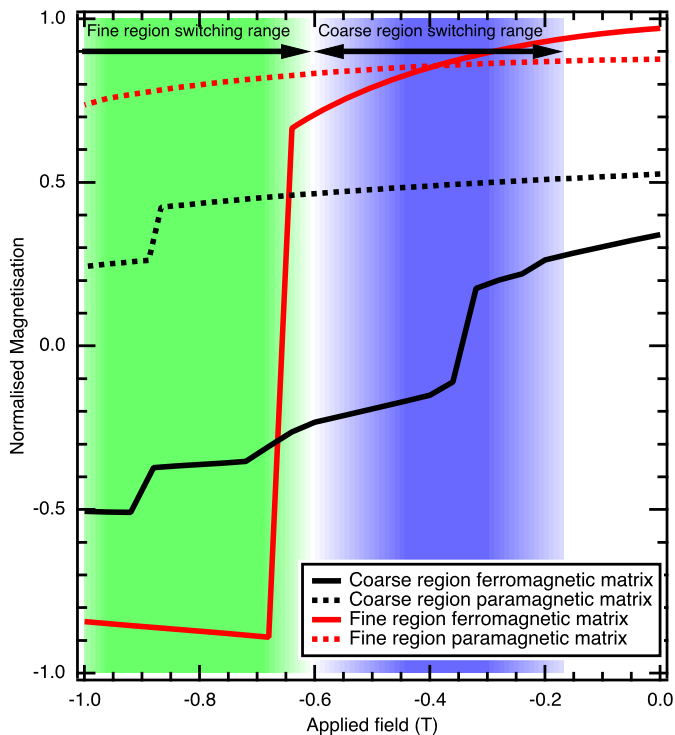
Fig. 8. Simulated upper branch of a hysteresis loop for both ferromagnetic and paramagnetic matrices in the coarse and fine CZ. The experimental switching range values have been included as a blue background for the coarse region and a green background for the fine region. Switching in both regions falls within the experimental ranges only when the matrix is ferromagnetic with a saturation magnetisation value approximately the same as that of tetrataenite. (For interpretation of the references to colour in this figure, the reader is referred to the web version of this article.)

4.2. Magnetic properties of the island/matrix nanocomposite

Micromagnetic simulations suggest that the CZ is best considered as a nanocomposite of exchange coupled magnetically hard and soft phases. Under certain circumstances, such systems can display exchange spring behaviour (Kneller and Hawig, 1991). Exchange springs have attracted considerable attention in the field of nanotechnology, as they offer the possibility to tune the magnetic properties of the composite by changing the relative proportions and dimensions of hard and soft phases (Asti et al., 2004). Reversible rotation of soft phase moments is observed up to a critical applied field value. Above this critical field value, which is significantly lower than the intrinsic hard phase switching field, magnetic domain walls penetrate and reverse the hard phase. The critical field value decreases as soft phase thickness increases (Fullerton et al., 1998). Experimental holography images show tetrataenite switching fields ranging from ∼0.2 T to 0.6 T in the coarse region, where the matrix is wide, and ∼0.6 T to 1.2 T in the fine region, where the matrix is narrow. These values are, for the most part, significantly lower than those predicted for isolated tetrataenite islands in our experimental geometry (∼1.2 T), and are in excellent agreement with hard/soft nanocomposite theory (Asti et al., 2004). The observed lowering of the coercivity in the coarse CZ could not be reproduced in the micromagnetic simulations without the addition of a soft magnetic matrix with the expected magnetic properties of ordered Fe_3Ni.

A unique feature of the tetrataenite islands from a paleomagnetic perspective is that, although the majority of islands (large and small) are uniformly magnetised in their remanent state (Fig. 7), they switch their magnetisation via the nucleation and propagation of domain walls. Islands within the bulk of the sample

demonstrated the behaviour predicted for a hard/soft nanocomposite (Asti et al., 2004), with domain walls forming in the soft matrix and penetrating into the hard phase at a critical field value. The range of switching field values within each region is attributed to variations in matrix thickness and stray fields that locally alter the applied field intensity.

According to exchange spring theory (Asti et al., 2004), when the soft phase thickness exceeds a critical value the system enters a 'decoupled magnet' regime. Once in this regime, the hard phase switching field value reaches its minimum value and no longer depends on the soft phase thickness. The magnetically soft and hard phase reversals are decoupled, so a reversed soft phase and unaffected hard phase can be observed simultaneously at remanence. This is the remanence state observed in the holography images for the soft magnetic strip at the sample surface caused by polishing (see supplementary information), confirming the bulk/surface system has entered the decoupled magnet regime.

The hard/soft nanocomposite observed here has profound implications for paleomagnetism. These systems display a reduction in the hard phase coercivity without reducing the thermal stability (Fullerton et al., 1998). Hence, a natural hard/soft nanocomposite, which the CZ is the first example of, is a fascinating exception to the paleomagnetic paradigm that thermal stability and coercivity are universally and intrinsically coupled (Dunlop and Ozdemir, 1997), i.e., the thermoremanent magnetisation (TRM) carrying capability will be significantly greater than that implied solely by coercivity measurements. Hence, we conclude that the CZ is an excellent nanoscale TRM carrier, with original moment directions stable in fields up to ∼0.5 T. Exchange spring behaviour also favours single-domain magnetic states within the hard phase, as exchange coupling to the uniformly magnetised matrix prevents magnetic domain walls from adopting an equilibrium position within a tetrataenite island (as observed in micromagnetic simulations of the CZ). This behaviour further enhances the TRM carrying capability of the larger CZ islands, that could otherwise display poor TRM carrying multidomain states.

4.3. Remanent magnetisation

As the CZ forms via a process of spinodal decomposition, the easy axis direction and magnetisation state adopted by each island has the potential to be influenced by an applied magnetic field. In other words, the CZ is capable of carrying a chemical transformation remanent magnetisation (CTRM, Dunlop and Ozdemir, 1997). If external influences are absent during spinodal decomposition, all six possible magnetisation directions would be expected to populate the islands with equal probability. A CTRM is manifested as a departure from this equally populated state. Given the high coercivity of individual tetrataenite islands, any remanence will remain stable for billions of years. Even if remagnetised in a strong field, some vestige of the original remanence (as evidenced by an uneven population of the three easy axes) may survive as long as the chemical nanostructure remains unaltered (Robinson et al., 2002). As the meteorite in this study is a fragment of the solidified core of an asteroid, it cannot contain any memory of a dynamo field that might have been present when the core was molten. It is more likely that the observed magnetic configuration is the result of local stray magnetic fields generated by neighbouring nanostructures (e.g. kamacite, plessite, or the tetrataenite rim). The field-of-view of the holography images is about 500 nm × 500 nm, which provides only a small sampling of the coarse and fine CZ. Hence, no firm conclusions can be drawn at this stage regarding the origin of such stray fields and whether they remain uniform on length scales beyond those investigated here.

The conclusions in this study pertain to CZs in general, which have been observed in chondrites (Uehara et al., 2011), pallasites (Yang et al., 2010) and mesosiderites (Yang et al., 1997b).

For metal originating from the unaltered crust of differentiated asteroids (Weiss and Elkins-Tanton, 2013), recent cooling models (Tarduno et al., 2012) predict that meteorites originating from the top 5–10% of a parent body (assuming an onion shell structure) will have reached the CZ formation temperature while the core was still molten. It is possible, in principle, to use statistical thermodynamics to relate the proportions of the six island states to the absolute field strength. A simple model (that ignores the influence of magnetic interactions between islands during formation), suggests that between 0–50% alignment could be achieved for 60 nm diameter islands and fields of 0–100 μT (Appendix A). Although in reality the degree of alignment is likely to be reduced by interactions, this preliminary analysis demonstrates that the CZ does have the potential to record CTRM at field strengths within the range proposed for asteroid dynamos. Furthermore, since the CZ formed sequentially over a period of 10–100 Ma as the metal cooled from ~320 °C to <100 °C (Fig. 1b), variations in CTRM across the CZ could be related to time variations of the asteroid dynamo field. The CTRM records relative changes in intensity and direction of the dynamo field, so could be used to study the existence of directional fluctuations, such as asteroid geomagnetic reversals analogous to those stored in the magnetic stripes within the Earth's spreading ocean crust. This record will also likely have overlapped with the solidification of the core and hence could be a means of studying the decay and eventual loss of dynamo activity.

5. Conclusions

1. The cloudy zones of meteoritic Fe–Ni metal correspond to a natural nanocomposite of magnetically hard tetrataenite islands and a magnetically soft matrix.
2. The matrix is composed of atomically ordered Fe_3Ni with the $L1_2$ structure.
3. The matrix magnetisation is similar in strength to that of tetrataenite in the coarse CZ and appears to decrease in intensity with increasing distance through the CZ.
4. Tetrataenite islands (up to the maximum ~100 nm diameter observed) display uniformly magnetised single domain states at remanence.
5. Switching occurs via the nucleation and propagation of domain walls through individual islands.
6. The coercivity of the coarse CZ is lowered due to exchange coupling to the soft matrix phase, which aids the nucleation and penetration of domain walls into the tetrataenite islands.
7. The tetrataenite easy axis of each island adopts one of three possible $\langle 001 \rangle$ orientations.
8. Magnetic fields influence the selection of the three easy axes and six corresponding magnetisation states as each CZ island forms, leading to a stable CTRM.
9. CZ formation in certain meteorites could have coincided with dynamo activity on planetesimals.
10. Progressive lateral development of the CZ during cooling could potentially encode time-resolved information regarding the planetesimal dynamo.

Acknowledgements

Appendix A. Statistical thermodynamics of island population

If the CZ is to record external fields of planetary intensities (10–100 μT), these fields must result in measurable differences in the proportions of the six possible magnetisation directions generated during ordering. To investigate this condition, we present a model which considers the energies associated with islands adopting any of the six possible easy axis directions in the presence of an arbitrary external field. Despite tetrataenite being a very magnetically hard material, fields of planetary intensity have the capability to influence the cubic $\langle 100 \rangle$ axis that becomes the tetrataenite c axis due to significant energy difference between the possible states in the presence of an applied field. When the tetrataenite islands first form they are isolated particles with a magnetisation $M = M_s V$, where M_s is the saturation magnetisation and V is the volume. For an external field $\mathbf{B} = (B_x, B_y, B_z)$, the energies of the six possible magnetisation directions (defined as $\pm x$, $\pm y$, $\pm z$) are:

$$E_{+x} = -MB_x \tag{1}$$

$$E_{-x} = MB_x \tag{2}$$

$$E_{+y} = -MB_y \tag{3}$$

$$E_{-y} = MB_y \tag{4}$$

$$E_{+z} = -MB_z \tag{5}$$

$$E_{+z} = MB_z \tag{6}$$

The total number of islands, N, can be expressed as the sum of the probabilities of thermally populating the six possible magnetisation directions:

$$N = e^{\frac{-MB_x}{k_B T}} + e^{\frac{MB_x}{k_B T}} + e^{\frac{-MB_y}{k_B T}} + e^{\frac{MB_y}{k_B T}} + e^{\frac{-MB_z}{k_B T}} + e^{\frac{MB_z}{k_B T}} \tag{7}$$

The average number of islands that will adopt a magnetisation direction along the positive x-direction can be expressed as a fraction of the total number of islands:

$$\frac{\langle n_{+x} \rangle}{N} = \frac{e^{\frac{-MB_x}{k_B T}}}{e^{\frac{-MB_x}{k_B T}} + e^{\frac{MB_x}{k_B T}} + e^{\frac{-MB_y}{k_B T}} + e^{\frac{MB_y}{k_B T}} + e^{\frac{-MB_z}{k_B T}} + e^{\frac{MB_z}{k_B T}}} \tag{8}$$

Similar expressions can be deduced for the remaining five magnetisation directions:

$$\frac{\langle n_{-x} \rangle}{N} = \frac{e^{\frac{MB_x}{k_B T}}}{e^{\frac{-MB_x}{k_B T}} + e^{\frac{MB_x}{k_B T}} + e^{\frac{-MB_y}{k_B T}} + e^{\frac{MB_y}{k_B T}} + e^{\frac{-MB_z}{k_B T}} + e^{\frac{MB_z}{k_B T}}} \tag{9}$$

$$\frac{\langle n_{+y} \rangle}{N} = \frac{e^{\frac{-MB_y}{k_B T}}}{e^{\frac{-MB_x}{k_B T}} + e^{\frac{MB_x}{k_B T}} + e^{\frac{-MB_y}{k_B T}} + e^{\frac{MB_y}{k_B T}} + e^{\frac{-MB_z}{k_B T}} + e^{\frac{MB_z}{k_B T}}} \tag{10}$$

$$\frac{\langle n_{-y} \rangle}{N} = \frac{e^{\frac{MB_y}{k_B T}}}{e^{\frac{-MB_x}{k_B T}} + e^{\frac{MB_x}{k_B T}} + e^{\frac{-MB_y}{k_B T}} + e^{\frac{MB_y}{k_B T}} + e^{\frac{-MB_z}{k_B T}} + e^{\frac{MB_z}{k_B T}}} \tag{11}$$

$$\frac{\langle n_{+z} \rangle}{N} = \frac{e^{\frac{-MB_z}{k_B T}}}{e^{\frac{-MB_x}{k_B T}} + e^{\frac{MB_x}{k_B T}} + e^{\frac{-MB_y}{k_B T}} + e^{\frac{MB_y}{k_B T}} + e^{\frac{-MB_z}{k_B T}} + e^{\frac{MB_z}{k_B T}}} \tag{12}$$

$$\frac{\langle n_{-z} \rangle}{N} = \frac{e^{\frac{MB_z}{k_B T}}}{e^{\frac{-MB_x}{k_B T}} + e^{\frac{MB_x}{k_B T}} + e^{\frac{-MB_y}{k_B T}} + e^{\frac{MB_y}{k_B T}} + e^{\frac{-MB_z}{k_B T}} + e^{\frac{MB_z}{k_B T}}} \tag{13}$$

Writing $\alpha = \frac{M_s V}{k_B T}$, the net number of islands along the x, y and z directions can be expressed respectively as:
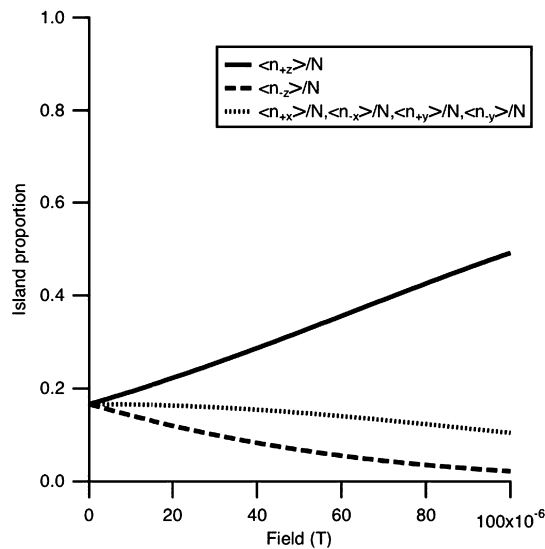
Fig. A.1. Results of the model described in Appendix A showing the proportion of the total number of islands with each of the 6 possible magnetisation directions. Islands had a 60 nm diameter and were magnetised at 320 °C in a field along the positive z-direction with a magnitude varying between 0 and 100 µT. $\langle n_{+x} \rangle = \langle n_{-x} \rangle = \langle n_{+y} \rangle = \langle n_{-y} \rangle$ as the field as been applied exactly along the z-direction and hence only one curve relating to all four proportions has been included. For this island size and temperature, proportions can vary between equal for all axes to 50% along the positive z-direction and 0% along the negative z-direction.

$$\frac{\langle n_{+x} \rangle - \langle n_{-x} \rangle}{N} = \frac{\sinh(\alpha B_x)}{\cosh(\alpha B_x) + \cosh(\alpha B_y) + \cosh(\alpha B_z)} \quad (14)$$

$$\frac{\langle n_{+y} \rangle - \langle n_{-y} \rangle}{N} = \frac{\sinh(\alpha B_y)}{\cosh(\alpha B_x) + \cosh(\alpha B_y) + \cosh(\alpha B_z)} \quad (15)$$

$$\frac{\langle n_{+z} \rangle - \langle n_{-z} \rangle}{N} = \frac{\sinh(\alpha B_z)}{\cosh(\alpha B_x) + \cosh(\alpha B_y) + \cosh(\alpha B_z)} \quad (16)$$

The Curie temperature for tetrataenite is ∼250 °C greater than it's ordering temperature (Dang and Rancourt, 1996), thus the variation of M_s with temperature across the CZ formation temperature range is assumed to be negligible and M_s is modelled as having a constant value close to that for 0 K (1300 emu cm^{-3}, Néel et al., 1964; James et al., 1999). The two important parameters are therefore the temperature and volume of the islands as they were magnetised. The temperature will range between 320 °C (when tetrataenite orders) and 200 °C where it is assumed that diffusion rates are too low for tetrataenite to form. The islands in the Tazewell range between ∼100 nm to <10 nm in diameter. Choosing an island diameter of 60 nm and an ordering temperature of 320 °C, the proportions of islands predicted by this model varies between 0 and 50% alignment to the field direction as the field varies between 0 and 100 µT (Fig. A.1). Hence fields of planetary intensity are expected to result in varying degrees of alignment with a measurable difference. It will also be possible to deduce the magnetising field from measurements of the proportions of the six possible easy axis directions using Eqs. (14), (15) and (16).

Appendix B. Supplementary material

Supplementary material related to this article can be found online at http://dx.doi.org/10.1016/j.epsl.2013.12.004.

References

Asti, G., Solzi, M., Ghidini, M., Neri, F.M., 2004. Micromagnetic analysis of exchange-coupled hard-soft planar nanocomposites. Phys. Rev. B 69 (17), 174401.

Beleggia, M., Zhu, Y., 2003. Electron-optical phase shift of magnetic nanoparticles I. Basic concepts. Philos. Mag. 83 (8), 1045–1057.

Bryson, J.F.J., Kasama, T., Dunin-Borkowski, R.E., Harrison, R.J., 2013. Ferrimagnetic/ferroelastic domain interactions in magnetite below the verwey transition: Part II. Micromagnetic and image simulations. Phase Transit. 86 (1), 88–102.

Dang, M.-Z., Rancourt, D.G., 1996. Simultaneous magnetic and chemical order-disorder phenomena in Fe$_3$Ni, FeNi, and FeNi$_3$. Phys. Rev. B 53 (5), 2291–2302.

Dunin-Borkowski, R.E., McCartney, M.R., Smith, D.J., 2004. Encyclopedia of Nanoscience and Nanotechnology. American Scientific Publishing.

Dunin-Borkowski, R.E., McCartney, M.R., Smith, D.J., Parkin, S., 1998. Toward quantitative electron holography of magnetic thin films using in situ magnetization reversal. Ultramicroscopy 74, 61–73.

Dunlop, D.J., Ozdemir, O., 1997. Rock Magnetism: Fundamentals to Frontiers. Cambridge University Press.

Evans, M.E., Krása, D., Williams, W., Winklhofer, M., 2006. Magnetostatic interactions in a natural magnetite–ulvöspinel system. J. Geophys. Res. 111 (B12), B12S16.

Feinberg, J.M., Harrison, R.J., Kasama, T., Dunin-Borkowski, R.E., Scott, G.R., Renne, P.R., 2006. Effects of internal mineral structures on the magnetic remanence of silicate-hosted titanomagnetite inclusions: An electron holography study. J. Geophys. Res. 111 (B12), B12S15.

Fu, R.R., Weiss, B.P., Shuster, D.L., Gattacceca, J., Grove, T.L., Suavet, C., Lima, E.A., Li, L., Kuan, A.T., 2012. An ancient core dynamo in asteroid Vesta. Science 338 (6104), 238–241.

Fullerton, E.E., Jiang, J.S., Grimsditch, M., Sowers, C.H., Bader, S.D., 1998. Exchange-spring behavior in epitaxial hard/soft magnetic bilayers. Phys. Rev. B 58 (18), 12193–12200.

Goldstein, J.I., Michael, J., 2006. The formation of plessite in meteoritic metal. Meteorit. Planet. Sci. 41 (4), 553–570.

Goldstein, J.I., Scott, E.R.D., Chabot, N.L., 2009. Iron meteorites crystallization, thermal history, parent bodies, and origin. Chem. Erde Geochem. 69 (4), 293–325.

Grabbe, E.M., 1940. Ferromagnetic anisotropy, magnetization at saturation, and superstructure in Ni$_3$Fe and nearby compositions. Phys. Rev. 57 (8), 728–734.

Harrison, R.J., Dunin-Borkowski, R., Putnis, A., 2002. Direct imaging of nanoscale magnetic interactions in minerals. Proc. Natl. Acad. Sci 99 (26), 16556–16561.

Howald, R.A., 2003. The thermodynamics of tetrataenite and awaruite: A review of the Fe–Ni phase diagram. Metall. Mater. Trans. A, Phys. Metall. Mater. Sci. 34A, 1759–1769.

James, P., Eriksson, O., Johansson, B., Abrikosov, I.A., 1999. Calculated magnetic properties of binary alloys between Fe, Co, Ni, and Cu. Phys. Rev. B 59 (1), 419–429.

Kneller, E.F., Hawig, R., 1991. The exchange-spring magnet: A new material principle for permanent magnets. IEEE Trans. Magn. 27 (4), 3588–3600.

Lappe, S.-C.L.L., Church, N.S., Kasama, T., Fanta, A.B.D.S., Bromiley, G., Dunin-Borkowski, R.E., Feinberg, J.M., Russell, S., Harrison, R.J., 2011. Mineral magnetism of dusty olivine: A credible recorder of pre-accretionary remanence. Geochem. Geophys. Geosyst. 12 (12).

Leroux, H., Doukhan, J.C., Perron, C., 2000. Microstructures of metal grains in ordinary chondrites: Implications for their thermal histories. Meteorit. Planet. Sci. 35, 569–580.

Maxwell, P.C., Goldberg, A., Shyne, J.C., 1974. Stress-assisted and strain-induced martensites in Fe–Ni–C alloys. Metall. Trans. 5 (6), 1305–1318.

Morito, H., Fujita, A., Fukamichi, K., Ota, T., Kainuma, R., Ishida, K., Oikawa, K., 2003. Magnetocrystalline anisotropy in a single crystal Fe–Ni–Ga ferromagnetic shape memory alloy. Mater. Trans. 44 (4), 661–664.

Néel, L., Pauleve, J., Pauthenet, R., Laugier, J., Dautreppe, D., 1964. Magnetic properties of nickel–iron alloys bombarded by neutrons in a magnetic field. J. Appl. Phys. 35 (3), 873–876.

Rancourt, D., Lagarec, K., Densmore, A., Dunlap, R., Goldstein, J., Reisener, R., Scorzelli, R., 1999. Experimental proof of the distinct electronic structure of a new meteoritic Fe–Ni alloy phase. J. Magn. Magn. Mater. 191, L225–L260.

Reuter, K., Williams, D., Goldstein, J., 1987. Low temperature phase transformations in the metallic phases of iron and stony–iron meteorites. Geochim. Cosmochim. Acta 52, 617–626.

Robinson, P., Harrison, R.J., McEnroe, S.A., Hargreaves, R.B., 2002. Lamellar magnetism in the haematite–ilmenite series as an explanation for strong remanent magnetization. Nature 418, 517–520.

Scheinfein, M., 1997. Llg micromagnetic simulator. http://llgmicro.home.mindspring.com.

Tarduno, J.A., Cottrell, R.D., Nimmo, F., Hopkins, J., Voronov, J., Erickson, A., Blackman, E., Scott, E.R.D., Mckinley, R., 2012. Evidence for a dynamo in the main group pallasite parent body. Science 338 (6109), 939–942.

Uehara, M., Gattacceca, J., Leroux, H., Jacob, D., van der Beek, C.J., 2011. Magnetic microstructures of metal grains in equilibrated ordinary chondrites and implications for paleomagnetism of meteorites. Earth Planet. Sci. Lett. 306 (3–4), 241–252.

Weiss, B.P., Elkins-Tanton, L.T., 2013. Differentiated planetesimals and the parent bodies of chondrites. Annu. Rev. Earth Planet. Sci. 41 (1), 529–560.

Weiss, B.P., Gattacceca, J., Stanley, S., Rochette, P., Christensen, U.R., 2010. Paleomagnetic records of meteorites and early planetesimal differentiation. Space Sci. Rev. 152, 341–390.

Yang, C.-W., Williams, D.B., Goldstein, J.I., 1997a. Low-temperature phase decomposition in metal from iron, stony–iron, and stony meteorites. Geochim. Cosmochim. Acta 61 (14), 2943–2956.

Yang, C.-W., Williams, D.B., Goldstein, J.I., 1997b. A new empirical cooling rate indicator for meteorites based on the size of the cloudy zone of the metallic phases. Meteorit. Planet. Sci. 32, 423–429.

Yang, J., Goldstein, J.I., 2005. The formation of the widmanstatten structure in meteorites. Meteorit. Planet. Sci. 40 (2), 239–253.

Yang, J., Goldstein, J.I., Scott, E.R.D., 2007. Iron meteorite evidence for early formation and catastrophic disruption of protoplanets. Nature 446 (7138), 888–891.

Yang, J., Goldstein, J.I., Scott, E.R.D., 2010. Main-group pallasites: thermal history, relationship to IIIAB irons, and origin. Geochim. Cosmochim. Acta 74, 4471–4492.